Structure and physical properties of CeSbTe

Ying C. Wang, Kristin M. Poduska, Roald Hoffmann[*], Francis J. DiSalvo[1]

Department of Chemistry and Chemical Biology, Baker Laboratory, Cornell University, Ithaca, NY 14853, USA

Abstract

The structure of CeSbTe was determined by the Rietveld refinement method using powder X-ray diffraction ($R_p = 6.22\%$ and $wR_p = 8.74\%$). CeSbTe adopts the PbFCl structure type and crystallizes in the space group *Pnma* (No. 62) of the orthorhombic system with $Z = 4$ and $a = 19.0404(6)$ Å, $b = 4.3520(1)$ Å, $c = 4.3660(2)$ Å, $V = 361.78(2)$ Å^3. It can be viewed as a layered compound which contains an Sb^{-1} layer distorted from a perfect square net into zig-zag chains. Both its crystallographic and electronic structure indicate a 2-D character. Based on transport properties and band structure calculations, CeSbTe is a metal with a low carrier concentration. Additionally, it exhibits paramagnetic behavior typical of Ce^{3+}. © 2001 Published by Elsevier Science B.V.

Keywords: Telluride; Thermoelectric; Rare earth metal; Square net; Electronic band structure

1. Introduction

Low-dimensional metals have opened a unique chapter in modern solid state science [1–6]. Among them, compounds containing 2-D square nets of main group elements which have varying degrees of distortion have displayed very interesting properties [7–11], for example, non-linear conductivity in $NbSe_3$ [7] and charge density waves (CDW) in layered rare-earth polychalcogenides [4,8–11].

Extensive studies have been conducted to address the Fermi surface nesting and CDW modulation in compounds containing 2-D square nets of main group elements [1,2,7–15]. In the family of square nets, the PbFCl structure type occupies a unique position; the bonding in the main group element layer in this structure ranges from ionic to metallic [11–15]. One group of compounds that crystallizes in this structure type is LnAB, where Ln is a rare earth metal and A and B are main group elements. Some LnAB compounds exhibit intriguing properties. For example, unusual electrical resistivity peaks and complex magnetic structures have been observed in $CeTe_2$ [16,17]. UAsSe has been found to be a 'single-impurity Kondo ferromagnet' [18,19]. Recently, there have been reports on the structure

and Fermi-surface driven CDW behaviors in $LaSb_xTe_{2-x}$ [9,10] and the crystal structure and electronic band structure of $LaTe_2$ [11].

CeSbTe, a member of LnAB, has been identified as a new phase [20], but full structural characterization and physical property studies of CeSbTe have not yet been reported. This paper presents our results on the crystallographic structure, transport properties, and electronic structure of CeSbTe.

2. Experimental

All manipulations were carried out in an argon-filled glove box. The starting materials were cerium ingots (Cerac) 99.9%, antimony shot (Alfa products) 99.999%, tellurium lumps (Cerac) 99.999%. Ce was purified by drip melting under vacuum in an RF furnace as described elsewhere [21].

Stoichiometric quantities of the elements were mixed in a vitreous carbon crucible (EMC), sealed in a silica tube, and heated at 750°C for 1 week. The sample was ground and pressed into a pellet in the presence of Ar; then it was annealed in a sealed silica tube at 700°C for 3 days.

Powder X-ray diffraction (Scintag XDS 2000, CuKα radiation at 25°C) was used to check phase purity. The X-ray powder pattern was similar to that of LaSbTe [9,10]. A Rietveld structural refinement on CeSbTe using GSAS [22] was based on the reported model of LaSbTe in space

*Corresponding author. Tel.: +1-607-255-7238; fax: +1-607-255-4137.

E-mail addresses: rh34@cornell.edu (R. Hoffmann), fjd3@cornell.edu (F.J. DiSalvo).

[1] Co-corresponding author.
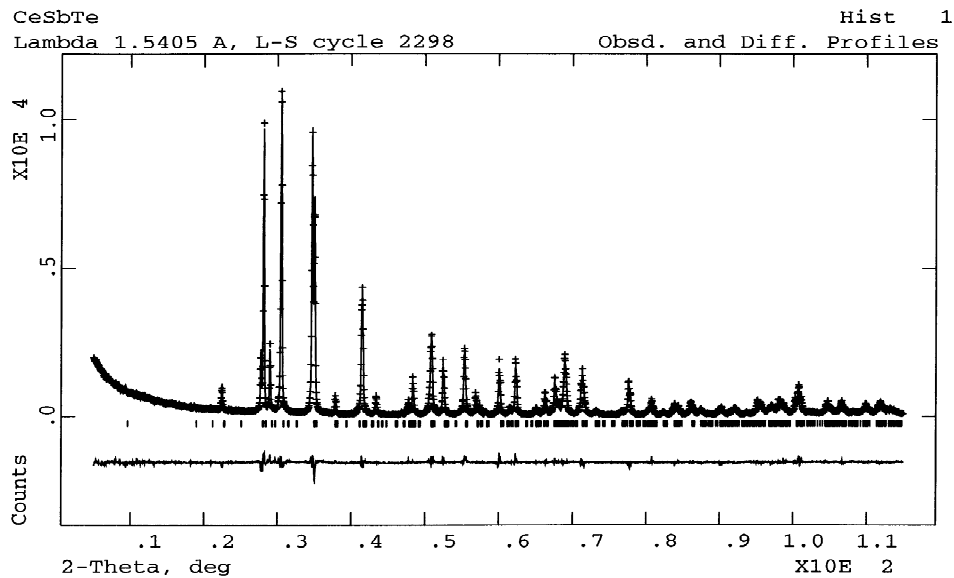
Fig. 1. Observed (+), calculated, and difference (bottom) X-ray powder diffraction pattern of CeSbTe by using GSAS (15).

group *Pnma* [9,10]. The plot of final profile refinement is shown in Fig. 1 with the relevant refinement information listed in Table 1. Structural data are tabulated in Tables 2 and 3.

Table 1
Crystal structure refinement information for CeSbTe

Compound	CeSbTe
Orthorhombic	
Pnma (62)	
a (Å)	19.0404(6)
b (Å)	4.3520(1)
c (Å)	4.3660(2)
Z	4
V (Å^3)	361.78(2)
Calculated density	7.151 gm/cm^3
Detector	HP Ge low-energy photon spectrometer
Counting time	5.5 s
Step	0.015
background	refined (Power series)
Profile function	pseudo-Voigt
Number of profile points	7333
Number of parameters refined	27
wR_p	0.0874
R_p	0.0622
R_B	0.0656
GOF	1.787
Durbin–Watson statistics	0.676

To measure the electrical resistivity and thermopower, the pellet was cut into a rectangular bar using a diamond-impregnated string saw (South Bay Tech.) and polished further by filing. The measurements were conducted by using a standard 4-probe AC method and a home-built thermopower measurement apparatus described elsewhere [23]. Silver epoxy (H20E, Epoxy Technology) was used to make electric contacts.

The remaining small pieces of the pellet were used for magnetic measurements on a Quantum Design MPMS SQUID magnetometer. The sample was cooled to low temperature at zero field and then the data were collected in a magnetic field of 11.6 kG as the sample warmed up.

Using the standard 4-probe method, the Hall coefficient of the polycrystalline sample of CeSbTe was measured at room temperature. After being cut to the dimensions $0.4 \times 2.0 \times 2.8$ mm using a diamond-impregnated string saw, a thin (≈ 1000 Å) layer of Au–Pd alloy was sputtered on to cover two opposite ends (for current contacts) and on two transverse spots (for resistance contacts) on the sample. Good electrical and physical contacts were then established between the sample and copper wire leads with silver epoxy (EPOTEK H20E). A Linear Research LR-700 AC resistance bridge supplied a 30 mA current at 16 Hz to the sample, and its resistance was measured repeatedly in zero gauss and 6500 gauss magnetic fields, with typical changes of resistance on the order of 0.1 μΩ. To correct for

Table 2
Atomic coordinates and isotropic displacement parameters (Å$^2 \times 100$)[a]

	x	y	z	U_{iso}
Ce	0.36143(4)	0.25	0.2639(6)	0.47(4)
Te	0.18658(5)	0.25	0.2639(7)	0.57(3)
Sb	0.50068(5)	−0.25	0.2341(6)	0.66(3)

[a] The U_{iso} is taken from the factor $\exp(-8\pi^2 U_{iso} \sin^2 \theta / \lambda^2)$.

Table 3
Selected bonding distances and bonding angles

Ce–Te	3.329(1), 3.215(3), 3.215(3)
Ce–Sb	3.432(1), 3.409(3), 3.420(3)
Sb–Sb	2.986(4), 3.182(4)
Sb–Sb–Sb	93.6(2)

Table 4
Slater-type orbital energies and exponents used in the extended Hückel calculation on CeSbTe

Atom	Orbital	H_{ii} (eV)	ζ_1	ζ_2	c_1	c_2
Ce	5d	−6.43	2.399	1.168	0.7477	0.3891
	6s	−4.97	1.398			
	6p	−4.97	1.398			
Sb	5s	−18.8	2.323			
	5p	−11.7	1.999			
Te	5s	−20.8	2.510			
	5p	−14.8	2.160			

magnetoresistive contributions to the Hall resistance, the resistance changes in forward and reverse fields were averaged.

Band structure calculations were performed using the 'Yet Another extended Hückel Molecular Orbital Package (YAeHMOP)' [24–28]. The extended Hückel parameters of Sb and Te listed in Table 4 are the standard atomic parameters from the package. The cerium parameters were obtained by using the procedure of Ortiz and Hoffmann [28]. The input geometries were based on the atomic parameters determined from the powder X-ray diffraction. A 126 k-point set in the irreducible wedge in the Brillouin zone was used to calculate average properties.

3. Results and discussion

3.1. Structure

CeSbTe adopts the same structure as CeAsS and LaSbTe, which is of the PbFCl type; many other compounds adopt this structure type, including Cu_2Sb and ZrSiS [12–15]. The CeSbTe unit cell parameters ($19.0404(6) \times 4.3520(1) \times 4.3660(2)$ Å^3) are smaller than those of LaSbTe (reported by DiMasi et al. to be $19.242(2) \times 4.3776(5) \times 4.4031(6)$ Å^3) due to the lanthanide contraction [9,10]. The compound can be viewed as a layered structure composed of distorted square nets of Sb, Te and Ce stacked along the x direction (Fig. 2) with a layer repeat sequence of Sb–Ce–Te–Te–Ce. The Sb layer is twice as dense as the Ce and Te layers.

Within the Ce net and the Te net, the nearest neighboring distances are 4.352 and 4.366 Å, respectively; no intra-net covalent bonding is expected in either net. Between neighboring Te layers, the Te–Te distance is 3.916 Å, much larger than the covalent bonding length 2.83 Å, but a little below the van der Waals contact of 4.06 Å [29–32]. Each Ce is coordinated by 4 Sb and 5 Te atoms, as shown in Fig. 3. Its coordination sphere can be described as a monocapped square antiprism. The Ce–Sb and Ce–Te distances fall within the range of 3.2–3.5 Å.
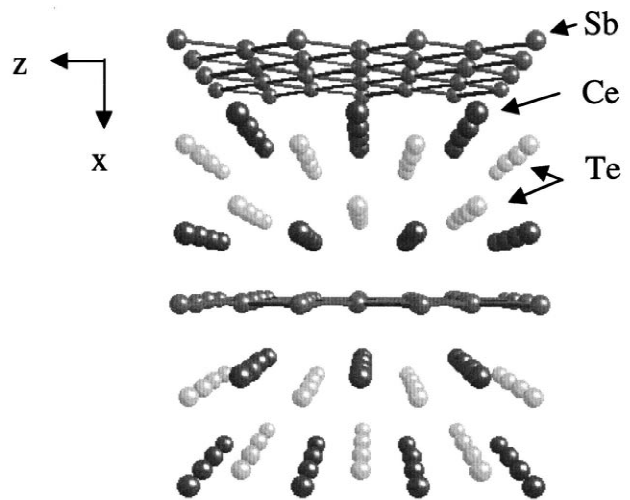
Fig. 2. The layered structure of CeSbTe.

When compared to the ionic radius sums of 3.54 Å for Ce–Sb and 3.32 Å for Ce–Te, the covalent radius sums of 3.05 Å for Ce–Sb and 3.01 Å for Ce–Te, and the atomic radius sums of 3.60 Å for Ce–Sb and 3.41 Å for Ce–Te [29–32], the range of bond distances we observe suggest that there is significant bonding between Ce and Sb or Te.

Within the Sb net, there are two different Sb–Sb distances (2.986 and 3.182 Å). Although these distances are larger than that of a typical Sb–Sb single bond (2.87 Å) [33–36], distances in the range of 2.9–3.3 Å are also
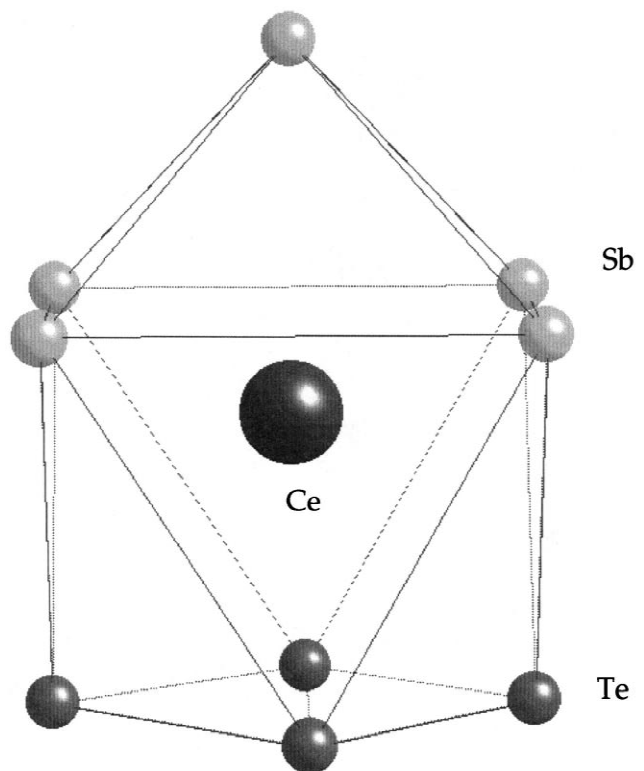
Fig. 3. The coordination of Ce by 4 Sb and 5 Te atoms.

found in other square net antimonides [9–14]. Clearly, some significant covalent Sb–Sb bonding occurs in the net. In fact, the Sb net in this compound can be viewed as a deformation from a perfect square net to infinite zig-zag chains running along the y axis (Fig. 4). The Sb–Sb distance inside the chain (2.986 Å) is shorter than the distance between the chains (3.182 Å), with a zigzag distortion of about 0.2 Å in the Sb layer. A similar distortion of 0.3 Å has been reported in LaSbTe [9,10]. This is one of the possible distortions from a square net to a lower symmetry that have been discussed in the literature [12–15].

Since Sb and Te are neighboring atoms showing no significant difference in X-ray diffracting power, bond valence analysis by EUTAX [33–36] was carried out to calculate the atomic valence sums at Sb and Te sites in order to support the original site assignment. In applying the valence analysis method, it is common that calculated apparent valences deviate from true valences, as discussed elsewhere [37,38]. It is the overall trend and comparison of the calculated valences that give information of structural
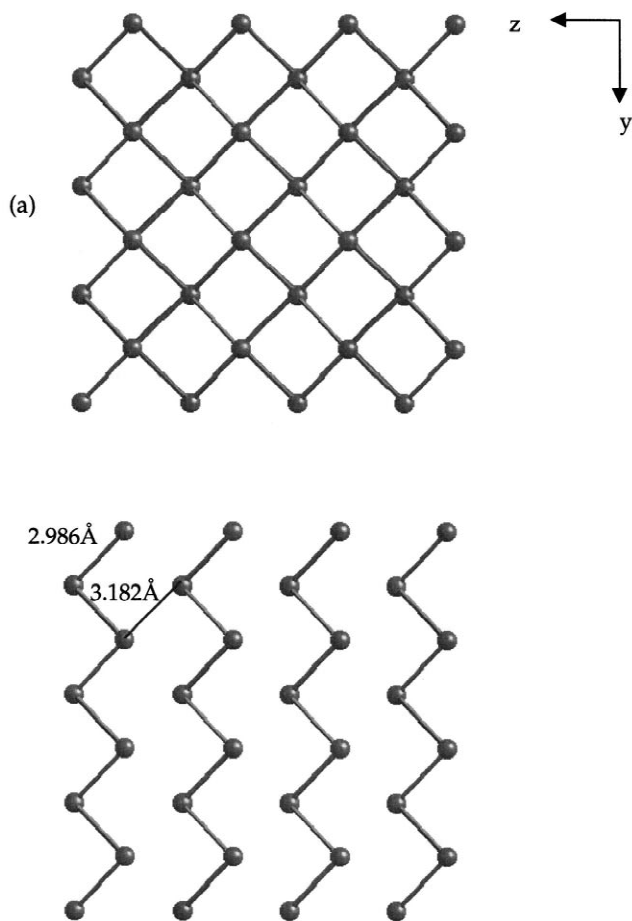
value. By using the Sb and Te assignment in the crystallographic structure (Table 2), the valence sums are found to be 3.488 at Sb and 2.133 at Te, which is in fair agreement with the atomic valences of 3 for Sb and 2 for Te (deviation smaller than 0.5). If Sb and Te are exchanged, the valence sums become 3.031 at Sb and 3.112 at Te. The calculated valence of Te would then significantly deviate from the true valence of 2 (deviation higher than 1). The site preference will be further investigated by calculations based on the extended Hückel tight binding method.

3.2. Magnetic properties

Fig. 5 shows the magnetic susceptibility χ and its inverse χ^{-1} as a function of temperature for CeSbTe. The increase of χ with decreasing T and the linear χ^{-1} vs. T behavior indicate that the compound is paramagnetic. A Curie–Weiss fit of data to $\chi = C/(T-\theta)$ above 85 K gives a magnetic moment of 2.49 μ_B per cerium and a θ value of -40 K. Considering that the magnetic moment of free Ce^{3+} ions is 2.54 μ_B, we can conclude that the cerium atom in CeSbTe is $3+$, which corresponds to the trivalence of La^{3+} in LaSbTe.

3.3. Transport properties

The electrical resistivity of the polycrystalline bar decreases from 2.9×10^{-3} Ω cm at room temperature to 0.97×10^{-3} Ω cm at 7.4 K (Fig. 6). The monotonically decreasing electrical resistivity with decreasing T suggests metallic behavior, but the change as a function of T is not as large as that of an atomically well ordered metal [39].

As shown in Fig. 7, the Seebeck coefficient drops from -46.7 μV/K at 300 K to -18.5 μV/K at 89.5 K. The negative sign indicates that electrons are the dominant carriers. For comparison, typical magnitudes of Seebeck

Fig. 4. Viewing the Sb layer as (a) a square net and (b) a distorted zig-zag chain by breaking the longer Sb–Sb bond. Compared with an ideal square net, the reflection plane along the y direction is lost in the distorted Sb layer.
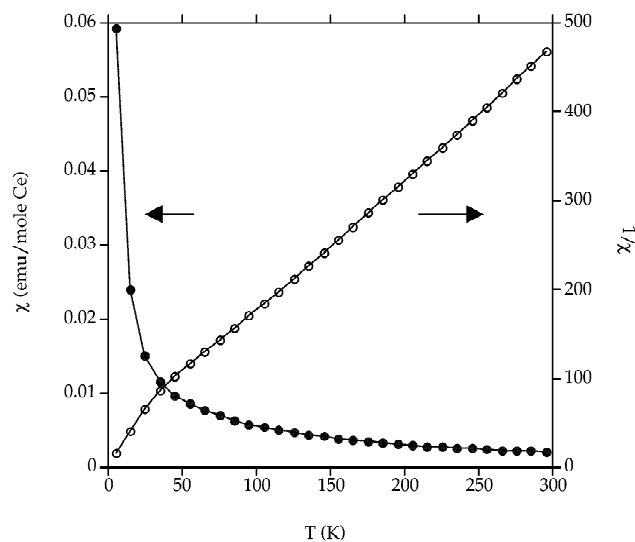
Fig. 5. χ and χ^{-1} as a function T for CeSbTe.
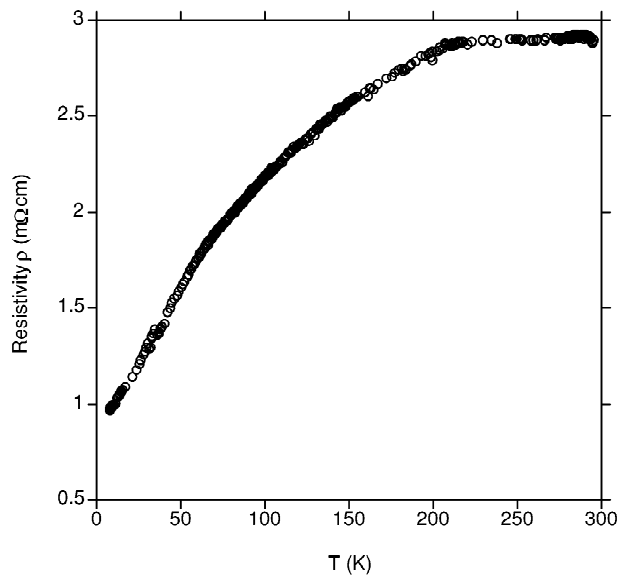
Fig. 6. Electrical resistivity as a function of T for CeSbTe.

coefficients at 300 K range from extremely small values (a few μV/K for metals), to 30–40 μV/K for some transition metal alloys, to 50–1000 μV/K for semiconductors [40,41]. Thus, the Seebeck coefficient of CeSbTe is on the boundary between metals and semiconductors, which is similar to the results observed for LaSbTe [42]. In contrast to CeTe$_2$ and UAsSe [16–19], no unusual behavior in transport properties was demonstrated in CeSbTe. Properties characteristic of Kondo effects or intermediate valence (IV) behavior were not observed.

The Hall coefficient R_H at room temperature was found to be $-4900 \pm 50 \times 10^{-13}$ V·cm/(A·G), which corresponds to a carrier density of -1.3×10^{20} e$^-$/cm^3. In agreement
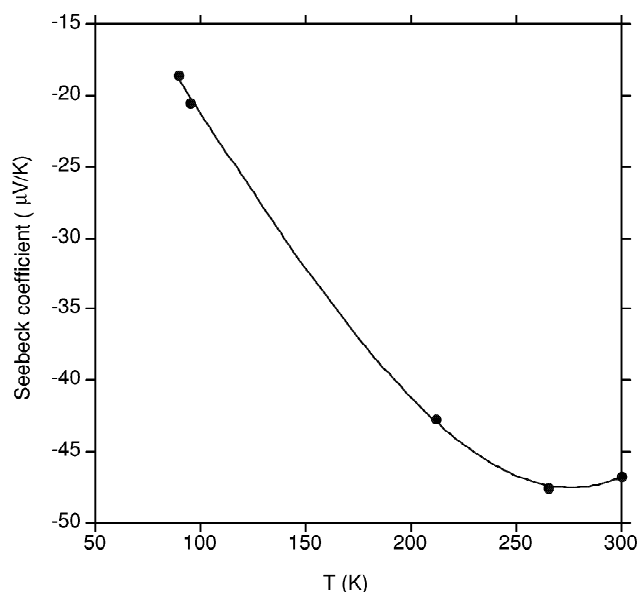
Fig. 7. Thermopower as a function of T for CeSbTe. The line shown is merely a guide to the eye.

with the Seebeck measurement, the Hall coefficient experiment confirms that electrons are the dominant carriers. The measured carrier density, consistent with the magnitude of resistivities and Seebeck coefficients, is characteristic of low carrier density systems.

The transport property measurements suggest that CeSbTe may be either a degenerate semiconductor or a poorly conducting metal. This ambiguity can be clarified by the electronic structure calculation of the compound using tight-binding extended Hückel methods.

3.4. Electronic structure calculations

How might one assign formal charges to the atoms in the CeSbTe? The electronegativities of the elements involved are not very different from each other; however, we can get a preliminary feeling for the charge distribution by using the Zintl–Klemm concept [43–46]. Based on the magnetism of CeSbTe, one $4f$ electron is localized on Ce; thus the Ce atom is in oxidation state $+3$. The electropositive element Ce can be considered as an electron donor; it formally transfers three electrons to the sublattice of $(SbTe)^{3-}$. Because Te atoms are surrounded by Ce and no Te–Te bonds are found, we can assign a -2 formal charge to Te. Te^{2-} then satisfies the classical octet rule. Therefore, Sb is left with a charge of -1, which is just the preferred electron count for a hypervalently bound square lattice [13].

A qualitative description of chemical bonding in the square net of Sb^{-1} goes as follows. The $5s$ and $5p_x$ orbitals of Sb (the latter perpendicular to the square net) are each filled with two electrons. The resulting bands are narrow and can be roughly considered as non-bonding. The $5p_y$ and $5p_z$ orbitals (in the plane of the net) give maximal bonding when they are occupied by one electron, forming two half-filled bands. This gives $6e^-$/Sb or Sb^{1-}. A calculation performed on the $(SbTe)^{3-}$ sublattice showed that the computed average net charges are actually close to these formal charges.

The calculations on the $(SbTe)^{3-}$ sublattice also indicate that the density-of-states (DOS) at the Fermi level (-6.73 eV) is entirely localized on the Sb sublattice. The DOS contribution from Sb spreads from about -23 eV all the way up to 7 eV, while the $5s$ and $5p$ contributions from Te remain well-localized below the Fermi level around their valence orbital ionization energies, $H_{5s5s} = -20.8$ eV and $H_{5p5p} = -14.8$ eV, respectively. It is no surprise that the stronger interactions are within the Sb layer: the Sb layer is twice as dense as the Te layer. Thus, the Sb site is more dispersive (shorter contact between the equivalent sites of that type [47]) than the Te site.

Since the calculations on the $(SbTe)^{3-}$ sublattice suggest that the electronic features at the Fermi level are determined by the Sb layers, it is worthwhile studying the electronic structures of these layers further. We performed calculations on a perfect square net and a distorted square

net both composed of Sb^{-1} in order to investigate the effects of the zig-zag distortion (0.2 Å distortion) on the electronic structure. The geometry distortion lowers the lattice symmetry; consequently, avoided crossings occur, as observed along the $\Gamma-Y$ symmetry line of the band structure of a perfect square net and a distorted square net (Fig. 8). The gap opening along $\Gamma-Y$ is related to the loss of mirror symmetry along the *y* direction. If we adjust the interchain distance (between the zig-zag Sb chains) to where the mirror symmetry is restored, then the gap along the line $\Gamma-Y$ closes. The magnitude of the DOS at the Fermi level also decreases by approximately two-thirds as a result of the zig-zag distortion. However, the 0.2 Å zig-zag distortion is not large enough to open a true band gap. The distorted square net composed of Sb^{-1} zig-zag chains remains metallic. In some separate calculations, we moved the zig-zag chains away from each other. As expected, at some point (where the interchain distance is around 5 Å), the layer becomes semiconducting, made up of weakly interacting classical one-dimensional Sb^{-1} chains.

In order to gauge the influence of Ce on the whole electronic structure of this compound, a calculation was performed on the full CeSbTe structure. The *4f* orbitals (occupied by one electron) are presumed not to participate in chemical bonding. These orbitals were not included in the calculation. That is, Ce is considered to have *6s*, *6p* and *5d* as valence orbitals with three valence electrons. To put it another way, the CeSbTe system is treated like LaSbTe; or, alternatively, from a fully ionic point of view, the $(SbTe)^{3-}$ unit is put together with $Ce^{3+}(4f)^1(5d)^0(6s)^0(6p)^0$.

The band structure of CeSbTe is shown in Fig. 9. The calculation on CeSbTe shows that the Fermi level lies at -8.70 eV, lower than the Fermi level of -6.73 eV for the $(SbTe)^{3-}$ sublattice. Obviously, there must be interaction between Ce and the (SbTe) substructure, lowering the Fermi level. The Fermi level cuts through a band, so this compound should be metallic. Along the symmetry lines U–Z and T–R (which are along the *x* direction), the band is pretty flat. On the other symmetry lines which cross over the *yz* plane, the band structure is highly dispersive. We also checked many other symmetry lines to see the band dispersion. Overall, the band structure displays more dispersion in the $k_y k_z$ plane than along the k_x direction. So while there is Ce–(SbTe) interaction, the compound remains two-dimensional.

The DOS of CeSbTe can be decomposed into Ce, Sb and Te contributions, as illustrated in Fig. 10. The Ce *6s* and *6p* contributions are unimportant in the range considered; their states lie much higher. About 85% of the Te contribution falls below the Fermi level, in some narrow *s* and *p* bands (Fig. 10). The other 15% Te contribution is found to be above the Fermi level; this is the result of Te interaction with Ce. The contributions from Ce and Sb both appear in the energy range of -23–8 eV (Figs. 10). A
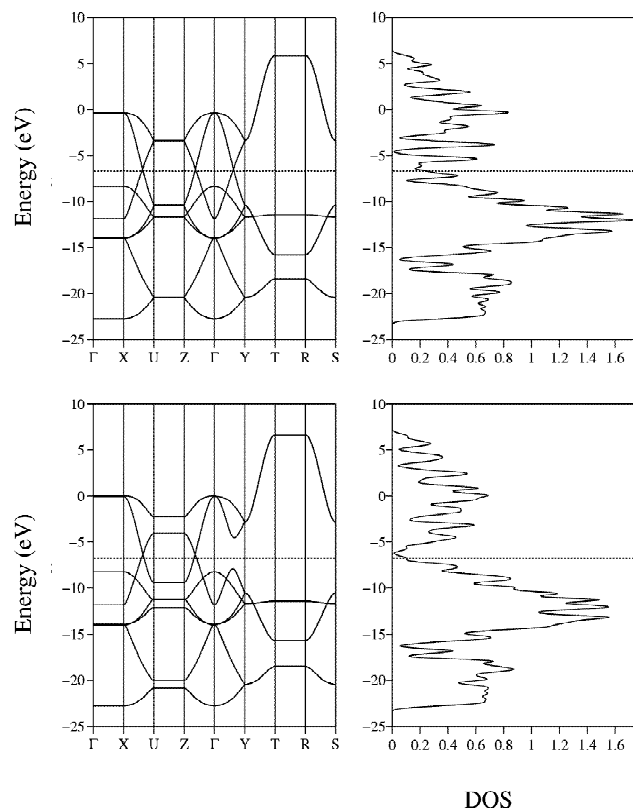
Fig. 8. Band structures (left) and DOS (right) of an Sb^{-1} ideal square net (top) and an Sb^{-1} distorted square net (bottom). For the sake of consistency and convenience of comparison with CeSbTe calculations, the unit cell settings are the sublattice Sb^{-1} of CeSbTe in Pnma; thus, there are four Sb atoms in each cell. $\Gamma(0,0,0)$, X(0.5,0,0), Y(0,0.5,0), Z(0,0,0.5), U(0.5,0,0.5), R(0.5,0.5,0.5), S(0.5,0.5,0), T(0,0.5,0.5).
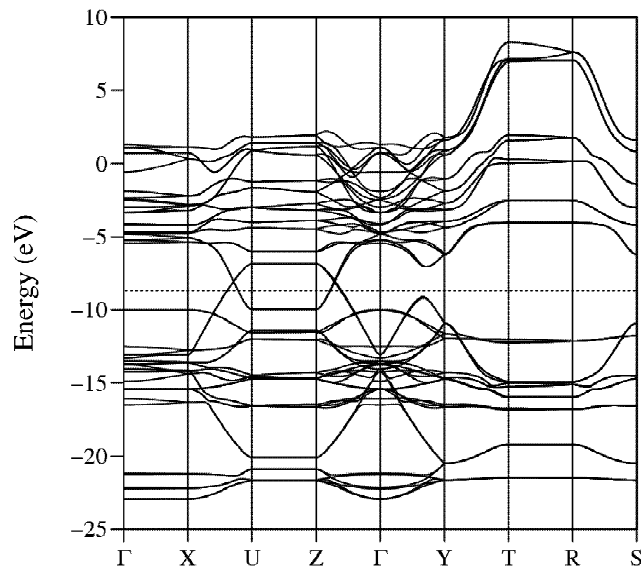
Fig. 9. Band structure of CeSbTe in the energy range of -25 to 10 eV. The dotted horizontal line indicates the Fermi level at -8.70 eV. $\Gamma(0,0,0)$, X(0.5,0,0), Y(0,0.5,0), Z(0,0,0.5), U(0.5,0,0.5), R(0.5,0.5,0.5), S(0.5,0.5,0), T(0,0.5,0.5).
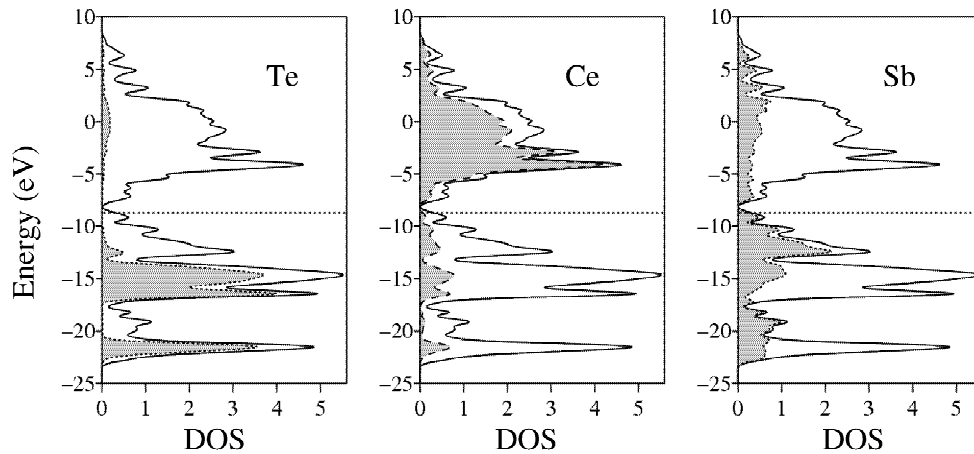
Fig. 10. The Te, Ce and Sb contributions to the DOS of CeSbTe in the energy range of −25 to 10 eV. The dotted horizontal line indicates the Fermi level at −8.70 eV.

small portion of Ce levels (about 10% of the total Ce contributions) is found between −23 and −10 eV, far below the Fermi level, due to the interaction of Ce with Sb and Te. Overall, a mixing of Ce orbitals with Sb and Te orbitals is observed. Note that the DOS at the Fermi level is dominated by not only Sb but also *5d* orbitals of Ce. Still the electronic structure indicates lower (two) dimensionality, and the driving force for distortion of the Sb square net remains.

The computed net charges from the calculation on CeSbTe are −0.21 for Sb, −0.86 for Te, and +1.07 for Ce. These charges are quite far from the formal charges of −1 for Sb, −2 for Te, and +3 for Ce. The result is not surprising if we consider the short contacts between Ce and Sb or Te and the moderate electronegativity difference (about 1) between Ce and Sb or Te. A comparison of the calculations performed on CeSbTe and on the $(SbTe)^{3-}$ sublattice clearly reveals the perturbation of Ce^{3+} on the $(SbTe)^{3-}$ sublattice and consequent charge transfer from the $(SbTe)^{3-}$ substructure to the Ce^{3+} cations. The Ce atoms are electropositive, yet involved in chemical bonding. They not only donate electrons but also interact with the neighboring Sb and Te atoms.

3.5. Discussion

One distinguishing feature in CeSbTe is the zig-zag distortion of Sb^{-1} square nets. The distortion of Sb^{-1} square nets into Sb^{-1} zig-zag chains can be understood in terms of a second-order Jahn–Teller distortion [1,2,12–14], Fermi surface nesting, or a CDW instability [3–6,9,10]. The non-vanishing DOS at the Fermi level in CeSbTe can be rationalized in terms of incomplete Fermi surface nesting. If the zig-zag distortion is so large that the net could be considered as a layer of non-interacting zig-zag chains (Sb^{-1}, like a Te chain), a band gap will be

open. This we actually probed in calculations, as mentioned above. Metallic properties are predicted from the band structure calculations performed on the full structure CeSbTe and the sublattice $(SbTe)^{3-}$. This is in accord with the conducting character demonstrated in transport property measurements. The low DOS at the Fermi level is also consistent with the poorly conducting metallic behavior and the low carrier concentration, 1.3×10^{20} e^-/cm^3. It is worth mentioning that LaSbTe does not have a high carrier concentration as typical metals do, based on the thermopower and electrical resistivity measurements on LaSbTe [42]. In addition, $CeTe_2$ [16,17] has been found to be an extremely low carrier system ($10^{14}-10^{15}$ cm^{-3}).

4. Conclusions

In summary, the structure of CeSbTe has been determined from powder X-ray diffraction. It is a layered compound with the layer repeat sequence Sb–Ce–Te–Te–Ce. One noteworthy structural feature is the 2-D Sb^{-1} net, which exhibits a distortion from a square net into zig-zag chains by a deformation of 0.2 Å. CeSbTe displays paramagnetic behavior related to Ce^{3+}. Additionally, CeSbTe can be formally described as Ce^{3+}, Te^{2-} and Sb^{1-}, which is confirmed by magnetic susceptibility measurements and electronic structure calculations. No *p–f* mixing or Kondo effects were observed in the transport property studies of CeSbTe. The distortion from Sb^{-1} square nets to zig-zag chains induced by Fermi surface nesting is not significant enough to open a band gap. A non-vanishing DOS is found at the Fermi level from the band structure calculation, which is in agreement with the metallic behavior observed in transport property measurements. The carrier concentration is moderately low (1.3×10^{20} e^-/cm^3), compared to typical metals which have carrier concentrations on the order of 10^{22} e^-/cm^3.

Acknowledgements

References

[1] M.-H. Whangbo, E. Canadell, J. Am. Chem. Soc. 114 (1992) 9587.
[2] E. Canadell, Chem. Mater. 10 (1998) 2770.
[3] J.A. Wilson, F.J. DiSalvo, S. Mahajan, Adv. Phys. 24 (1975) 117.
[4] P.M. Williams, in: F. Lévy (Ed.), Crystallography and Crystal Chemistry of Materials with Layered Structures, D. Reidel, Dordrecht, Vol. 2, 1976, p. 51.
[5] J. Ferraris, D.O. Cowan, V.V. Walatka, J.H. Perlstein, J. Am. Chem. Soc. 95 (1973) 948.
[6] L.B. Coleman, M.J. Cohen, D.J. Sandman, F.G. Yamagishi, A.F. Garito, A.J. Heeger, Solid State Commun. 12 (1973) 1125.
[7] P. Monceau, N.P. Ong, A.M. Portis, A. Meerschaut, J. Rouxel, Phys. Rev. Lett. 37 (1976) 602.
[8] B. Foran, S. Lee, M.C. Aronson, Chem. Mater. 5 (1993) 974.
[9] E. DiMasi, M.C. Aronson, J.F. Mansfield, B. Foran, S. Lee, Phys. Rev. Lett. Rev. B 52 (1995) 14516.
[10] E. DiMasi, B. Foran, M.C. Aronson, S. Lee, Phys. Rev. B 54 (1996) 13587.
[11] K. Stöwe, J. Solid State Chem. 149 (2000) 155.
[12] W. Tremel, R. Hoffmann, J. Am. Chem. Soc. 109 (1987) 124.
[13] G. Papoian, R. Hoffmann, Angew. Chem. Int. Ed. 39 (2000) 2409.
[14] G. Papoian, R. Hoffmann, J. Solid State Chem. 139 (1998) 8.
[15] F. Hulliger, R. Schmelczer, D. Schwarzenbach, J. Solid State Chem. 21 (1977) 371.
[16] Y.S. Kwon, T.S. Park, K.R. Lee, J.M. Kim, Y. Haga, T. Suzuki, J. Magn. Magn. Mater. 140–144 (1995) 1173.
[17] M.H. Jung, Y.S. Kwon, T. Suzuki, Physica B 240 (1997) 83.
[18] Z. Henkie, R. Fabrowski, A. Wojakowski, J. Alloys Comp. 219 (1995) 248.
[19] Z. Henkie, T. Cichorek, A. Pietraszko, R. Fabrowski, A. Wojakowski, B.S. Kuzhel, L. Kepinski, L. Krajczyk, A. Gukasov, P. Wisniewski, J. Phys. Chem. Solids 59 (1998) 385.
[20] J.-P. Charvillat, D. Damien, A. Wojakowski, Revue de Chimie Minérale 14 (1977) 178.
[21] R.A. Gordon, Y. Ijiri, C.M. Spencer, F.J. DiSalvo, J. Alloys Comp. 224 (1995) 101.
[22] A.C. Larson, R.B. Von Dreele, General Structure Analysis System, Los Alamos National Laboratory.
[23] C.D.W. Jones, K.A. Regan, F.J. DiSalvo, Phys. Rev. B58 (1998) 16057.
[24] R. Hoffmann, J. Chem. Phys. 39 (1963) 1397.
[25] R. Hoffmann, W.N. Lipscomb, J. Chem. Phys. 37 (1962) 2872.
[26] J.H. Ammeter, H.-B. Bürgi, J.C. Thibeault, R. Hoffmann, J. Am. Chem. Soc. 100 (1978) 3686.
[27] G.A. Landrum, http://overlap.chem.cornell.edu:8080/yaehmop.html (1995).
[28] J.V. Ortiz, R. Hoffmann, Inorg. Chem. 24 (1985) 2095.
[29] A.J. Ashe III, E.G. Ludwig Jr., J. Oleksyzyn, J.C. Huffman, Organometallics 3 (1984) 337.
[30] U. Müller, in: Inorganic Structural Chemistry, 3rd Edition, John Wiley and Sons, UK, 1994, p. 96.
[31] U. Müller, in: Inorganic Structural Chemistry, John Wiley and Sons, UK, 1994, p. 31.
[32] Table of Periodic Properties of the Elements, Sargent-Welch Scientific Company.
[33] M. O'Keeffe, N. Brese, Program EUTAX 1.2, 1992.
[34] N.E. Brese, M. O'Keeffe, Acta Cryst. B47 (1991) 192.
[35] M. O'Keeffe, N.E. Brese, Acta Cryst. B48 (1992) 152.
[36] M. O'Keeffe, N.E. Brese, J. Am. Chem. Soc. 113 (1991) 3226.
[37] M. O'Keeffe, Structure and Bonding 71 (1989) 162.
[38] Y.C. Wang, F.J. DiSalvo, Chem. Mater. 12 (2000) 1011.
[39] N.W. Ashcroft, N.D. Mermin, in: Solid State Phys., Holt, Rinehart and Winston, USA, 1976, p. 8.
[40] I.B. Cadoff, E. Miller, in: Thermoelectric Matierials and Devices, Reinhold Publishing Corporation, New York, 1960, p. 57, Chapter 5.
[41] D.D. Pollock, in: Encyclopedia of Physical Science and Technology, Vol. 16, Academic Press Inc., 1992, p. 657.
[42] K.S.V.L. Narasimhan, H. Steinfink, Mater. Sci. Eng. 3 (1968–1969) 309.
[43] E. Zintl, W. Dullenkopf, Z. Phys. Chem. B 16 (1932) 183.
[44] E. Zintl, G. Brauer, Z. Phys. Chem. B 20 (1933) 245.
[45] E. Zintl, Angew. Chem. 52 (1939) 1.
[46] W. Klemm, Z. Anorg. Allg. Chem. 247 (1941) 1.
[47] C. Zheng, R. Hoffmann, R. Nesper, H. von Schnering, J. Am. Chem. Soc. 108 (1986) 1876.